



**HAL**  
open science

# Coronal mass ejection kinematics deduced from white light (Solar Mass Ejection Imager) and radio (Wind/WAVES) observations

M. J. Reiner, Bernard V. Jackson, D. F. Webb, D. R. Mizuno, Michael L. Kaiser, Jean-Louis Bougeret

## ► To cite this version:

M. J. Reiner, Bernard V. Jackson, D. F. Webb, D. R. Mizuno, Michael L. Kaiser, et al.. Coronal mass ejection kinematics deduced from white light (Solar Mass Ejection Imager) and radio (Wind/WAVES) observations. *Journal of Geophysical Research Space Physics*, 2005, 110, 10.1029/2004JA010943 . hal-03742221

**HAL Id: hal-03742221**

**<https://hal.science/hal-03742221>**

Submitted on 20 Aug 2022

**HAL** is a multi-disciplinary open access archive for the deposit and dissemination of scientific research documents, whether they are published or not. The documents may come from teaching and research institutions in France or abroad, or from public or private research centers.

L'archive ouverte pluridisciplinaire **HAL**, est destinée au dépôt et à la diffusion de documents scientifiques de niveau recherche, publiés ou non, émanant des établissements d'enseignement et de recherche français ou étrangers, des laboratoires publics ou privés.

Copyright

## Coronal mass ejection kinematics deduced from white light (Solar Mass Ejection Imager) and radio (Wind/WAVES) observations

M. J. Reiner,<sup>1</sup> B. V. Jackson,<sup>2</sup> D. F. Webb,<sup>3</sup> D. R. Mizuno,<sup>3</sup> M. L. Kaiser,<sup>4</sup> and J.-L. Bougeret<sup>5</sup>

Received 1 December 2004; revised 11 May 2005; accepted 20 May 2005; published 30 September 2005.

[1] White-light and radio observations are combined to deduce the coronal and interplanetary kinematics of a fast coronal mass ejection (CME) that was ejected from the Sun at about 1700 UT on 2 November 2003. The CME, which was associated with an X8.3 solar flare from W56°, was observed by the Mauna Loa and Solar and Heliospheric Observatory (SOHO) Large-Angle Spectrometric Coronagraph (LASCO) coronagraphs to 14  $R_{\odot}$ . The measured plane-of-sky speed of the LASCO CME was 2600 km s<sup>-1</sup>. To deduce the kinematics of this CME, we use the plane-of-sky white light observations from both the Solar Mass Ejection Imager (SMEI) all-sky camera on board the Coriolis spacecraft and the SOHO/LASCO coronagraph, as well as the frequency drift rate of the low-frequency radio data and the results of the radio direction-finding analysis from the WAVES experiment on the Wind spacecraft. In agreement with the in situ observations for this event, we find that both the white light and radio observations indicate that the CME must have decelerated significantly beginning near the Sun and continuing well into the interplanetary medium. More specifically, by requiring self-consistency of all the available remote and in situ data, together with a simple, but not unreasonable, assumption about the general characteristic of the CME deceleration, we were able to deduce the radial speed and distance time profiles for this CME as it propagated from the Sun to 1 AU. The technique presented here, which is applicable to mutual SMEI/WAVES CME events, is expected to provide a more complete description and better quantitative understanding of how CMEs propagate through interplanetary space, as well as how the radio emissions, generated by propagating CME/shocks, relate to the shock and CME. This understanding can potentially lead to more accurate predictions for the onset times of space weather events, such as those that were observed during this unique period of intense solar activity.

**Citation:** Reiner, M. J., B. V. Jackson, D. F. Webb, D. R. Mizuno, M. L. Kaiser, and J.-L. Bougeret (2005), Coronal mass ejection kinematics deduced from white light (Solar Mass Ejection Imager) and radio (Wind/WAVES) observations, *J. Geophys. Res.*, *110*, A09S14, doi:10.1029/2004JA010943.

### 1. Introduction

[2] The solar events that occurred in late October and early November of 2003 (“Halloween Events”) included some of the most energetic events of solar cycle 23. Although there were some intense flares associated with

active region NOAA 0486 from 22 October 2003, the main series of events of interest here commenced with an X17.2 class flare on 28 October 2003 and ended with an X28 class flare on 4 November 2003. Most of these events were associated with intense long-duration soft X-ray events (LDEs); many also had significant hard X-ray fluxes observed by Reuven Ramaty High Energy Solar Spectroscopic Imager (RHESSI). Most of the large (>M3.0) X-ray events were associated with very intense and complex type II, III, and IV radio emissions, observed over a very wide range of radio frequencies by both ground- and space-based radio receivers. All of these events had associated fast coronal mass ejections (CMEs) that were observed near the Sun by ground- and space-based coronagraphs. The majority of these X-ray flare/CME events were associated with the active region NOAA 0486, which rotated from W02° to W83° during this period of enhanced solar activity. The resulting propagating interplanetary disturbances had major

<sup>1</sup>Catholic University of America and NASA Goddard Space Flight Center, Greenbelt, Maryland, USA.

<sup>2</sup>Center for Astrophysics and Space Sciences, University of California, San Diego, California, USA.

<sup>3</sup>Institute for Scientific Research, Boston College, Chestnut Hill, Massachusetts, USA.

<sup>4</sup>Solar System Exploration Division, NASA Goddard Space Flight Center, Greenbelt, Maryland, USA.

<sup>5</sup>Observatoire de Paris, Laboratoire d’Etudes Spatiales et d’Instrumentation en Astrophysique, Meudon, France.

space weather repercussions at Earth, as indicated by very low *Dst* values and/or high solar energetic particle fluxes.

[3] The characterization of the interplanetary transport of CMEs is critical for predicting the potential onset of space weather events. Comparisons of the near-Sun, plane-of-sky CME speeds, mean transit times, and in situ shock speeds have clearly, but indirectly, revealed that CMEs generally decelerate as they propagate through interplanetary space [Gosling *et al.*, 1968, 1975; Schwenn, 1983; St. Cyr *et al.*, 2000]. A crucial issue then is to quantify where and how CMEs decelerate. Initial Solar and Heliospheric Observatory (SOHO) Large-Angle Spectrometric Coronagraph (LASCO) investigations revealed little evidence for significant deceleration for most CMEs within the LASCO field of view to  $30 R_{\odot}$ : a linear (constant speed) fit to the height-time data was usually found to provide an adequate fit to within the measurement uncertainties [St. Cyr *et al.*, 2000]. This suggests that either the deceleration is relatively small and/or that much of the CME deceleration may occur beyond  $30 R_{\odot}$ . Using the observed CME transit speeds, Gopalswamy *et al.* [2000, 2001a] and Michalek *et al.* [2004] deduced that the CME deceleration was indeed expected to be relatively small for most CMEs and that the CME deceleration was directly correlated with the near-Sun (initial) CME speed, the faster CMEs clearly tending to decelerate more rapidly. Although CME acceleration is difficult to directly measure within the LASCO field of view due to the uncertainties of the measured height values and to the limited number of height-time values available for the faster CMEs, statistical analyses for large samples of LASCO events do show a definite increase in measured apparent deceleration with CME initial speed, consistent with the above investigations [Yashiro *et al.*, 2004].

[4] These results demonstrate that to directly quantify the coronal and interplanetary transport of CMEs, white light observations beyond the  $32 R_{\odot}$  limit of the LASCO coronagraph are needed. The Solar Mass Ejection Imager (SMEI) on the Air Force Coriolis satellite, launched on 6 January 2003, is the first all-sky white light camera specifically designed for imaging and tracking of CMEs in interplanetary space [Eyles *et al.*, 2003; Jackson *et al.*, 2005b]. Fortuitously, the all-sky (SMEI) camera observed the interplanetary extension of many of the LASCO CMEs associated with the “Halloween” events [see Jackson *et al.*, 2005a].

[5] Nevertheless, there is a relatively large spatial gap between the LASCO ( $<32 R_{\odot}$ ) and the SMEI ( $>70 R_{\odot}$ ) white light observations. Consequently, it is often difficult to accurately determine the precise CME kinematics consistent with these data. Radio observations, on the other hand, can bridge the current spatial gap in the white light observations. Indeed, radio observations have long been used to deduce the kinematics of CME/shocks in the corona and interplanetary medium.

[6] Interplanetary radio scintillation (IPS) measurements have been used to trace CMEs beyond the coronagraph field of view. These IPS measurements, like the white light observations, are plane-of-sky measurements, so they can significantly underestimate the dynamics of off-limb CME events. Doppler scintillation measurements, when compared with in situ plasma data from various spacecraft, have revealed that fast CMEs decelerate rapidly near the Sun

[Woo *et al.*, 1985]. More specifically, the faster CMEs exhibited greater deceleration but for shorter time periods. By contrast, more recent scintillation analyses, applied to the Bastille Day event, suggested a two-staged deceleration, with moderate deceleration to  $\sim 0.5$  AU, followed by a much more rapid deceleration beyond  $0.5$  AU [Manoharan *et al.*, 2001].

[7] Another signature of the coronal and interplanetary transport of CMEs are the type II radio bursts [Payne-Scott *et al.*, 1947; Cane *et al.*, 1982, 1987]. The observed frequency drift rate of type II radio emissions, generated by coronal and/or CME-driven shocks, provides a direct measure of the coronal or interplanetary shock speed [see, e.g., Wild, 1954; Robinson, 1985]. These frequency-drifting radio bursts can, in principal, provide continuous tracking of a CME/shock from the solar corona all the way to  $1$  AU (and beyond). Since these radio observations depend directly on the plasma density in the source region, which in turn is related to the heliocentric distance, these radio measurements relate directly to the “true” radial CME speed and “true” acceleration. Preliminary results on the interplanetary transport of CMEs, provided by the low-frequency (kilometric) radio observations, have suggested that CMEs exhibit significant acceleration out to about  $60 R_{\odot}$  and then exhibit significant deceleration [Cane, 1983].

[8] More recently, Reiner *et al.* [2001, 2003b] developed a technique for deducing the radial speed and (heliocentric) distance time profiles for individual CMEs from the solar corona to  $1$  AU. This method utilizes both the measured in situ shock speed and the measured frequency drift rate of the associated type II radio emissions, while making simplifying, but realistic, assumptions about the nature of the deceleration (constant deceleration, followed by constant speed) and about the density-distance scale. Application of this technique to a large number of CME events can provide insights into how CMEs decelerate as they propagate through the interplanetary medium and how a given CME speed profile depends on the initial CME parameters and on the conditions in the interplanetary medium [Reiner and Kaiser, 2002]. Information on the effective drag force that determines the CME dynamics can also be extracted from these analyses [Reiner *et al.*, 2003b].

[9] The purpose of this paper is to apply this technique to a CME event for which there were white light observations from both SMEI and LASCO. We will demonstrate how the constraints provided by the white light images and the low-frequency radio data from Wind/WAVES can be combined to quantify the propagation characteristics of the CME/shock through the corona and interplanetary space, as well as to provide information and insights into the location of radio emitting regions of the shock front. For various reasons the combined WAVES and SMEI observations lends itself best to the 2 November 2003 CME event that occurred near the end of the sequence of “Halloween” events.

[10] Specifically, the measured shock speed at  $1$  AU and the transit time are used to derive possible radial speed and distance profiles for the CME/shock. The elongation angle-time measurements from SMEI and the frequency drift of the low-frequency radio emissions are then used to select those speed/distance profiles that provide the best simultaneous fit to these data. Finally, the elongation angles of the

centroids of the radio sources at different times and at different frequencies, derived using the direction-finding capabilities on Wind/WAVES, are compared directly with the elongations of the CME/shock to provide insights into the relationship of the radio sources to the CME and its associated shock. This is the first time that the analyses of the SMEI white light images or the radio direction finding have been used, together with the radio frequency drift rate, to provide constraints on the interplanetary propagation of a CME/shock. By requiring self-consistency between these diverse data, we believe that realistic estimates of the complete speed and distance time profiles of the CME over the entire distance range from the Sun to 1 AU are obtained, in spite of limitations and uncertainties inherent in each of the white light and radio observations separately.

## 2. SMEI and WAVES Instrumentation

[11] The SMEI “all-sky” camera on the Coriolis spacecraft has provided the first high spatial and temporal resolution white light images of CMEs beyond about  $70 R_{\odot}$  [Tappin *et al.*, 2004]. This instrument consists of 3 CCD cameras each observing a strip of sky approximately  $60^{\circ} \times 3^{\circ}$  through a baffle which minimizes stray light [Eyles *et al.*, 2003; Jackson *et al.*, 2005b]. The cameras are arranged on the spacecraft such that in the course of a 102-min Sun-synchronous polar orbit along Earth’s terminator almost the full  $4\pi$  sr of the sky, except for small regions close to the Sun and in the antisolar direction, is observed. Interplanetary disturbances are detected by looking for variations in the intensity of the Thomson-scattered light caused by the density enhancements and depletions of the disturbances. Three-dimensional (3-D) reconstruction techniques are being developed to clean the images and track and analyze the detailed density structures of the CME. These techniques have been previously demonstrated by Jackson and collaborators [Jackson and Hick, 2004; Jackson *et al.*, 2005a].

[12] The WAVES experiment on the Wind spacecraft, which was launched 10 years ago in November of 1994, has been monitoring solar radio emissions, with high-time and -frequency resolution, during the complete rise and fall of solar cycle 23. These unique radio observations have led to many new discoveries and insights related to solar energetic phenomena: relationship of the type II radio source to interplanetary structures [Reiner *et al.*, 1998a]; shock associated (SA) bursts [Bougeret *et al.*, 1998; Dulk *et al.*, 2000]; complex type III bursts [Reiner and Kaiser, 1999; Reiner *et al.*, 2000a]; U-bursts [Leblanc *et al.*, 1999]; relation of coronal to interplanetary shocks [Reiner *et al.*, 2000b, 2003a]; CME interactions [Gopalswamy *et al.*, 2001b]; low-frequency (continuum) type IV bursts [Leblanc *et al.*, 2000]; SEP–radio relationships [Gopalswamy *et al.*, 2002; Cane *et al.*, 2002; Cane and Erickson, 2003; Cane, 2003]; etc.

[13] This instrument includes several radio receivers that cover the frequency range from 4.0876 kHz to 13.825 MHz [Bougeret *et al.*, 1995]. The instruments used in the present analysis were the superheterodyne (step-tuned) receivers: RAD2, which normally sweeps 256 frequency channels from 1.075 to 13.825 MHz in 16.192 s with a frequency resolution of 50 kHz, and RAD1, which covers the fre-

quency range from 20 to 1040 kHz at 32 discrete frequencies (selected from 256 frequency channels) with a highest sampling rate of 45.8 s. The RAD1 receivers are connected to a dipole antenna (50 m elements) in the spacecraft spin plane and a dipole antenna (5.28 m elements) along the spacecraft spin axis, and the RAD2 receivers are connected to a dipole antenna (7.5 m elements) in the spacecraft spin plane, in addition to the spin axis antenna. During the time of the event discussed here, Wind was located in the far Geotail at  $(-175, -25, -4) R_E$  Geocentric Solar Ecliptic (GSE) coordinates.

## 3. CME Kinematics Deduced From Remote and In Situ Observations

[14] The 2 November 2003 CME was associated with a solar X8.3 soft X-ray flare observed from 1703 to 1739 UT, with maximum at 1725 UT. There was an associated 2B  $H_{\alpha}$  flare from NOAA 0486 located at  $S14^{\circ}W56^{\circ}$ . Various characteristic radio emissions (type II, III, and IV bursts) were reported by ground-based observatories in association with this major solar event. The arrival of the associated CME-driven shock and ejecta at Earth on 4 November 2003 caused the *Dst* to dip to  $-89$  (nT); the *Kp* index was greater than 5 for a 6-hour period. As expected, this western event also produced a high flux of solar energetic particles (SEP).

### 3.1. Constraints on CME Kinematics From LASCO White-Light Observations and 1 AU Solar Wind Measurements

[15] Owing to the very high speed of this CME, only three height-time values of the CME leading edge could be measured in the LASCO coronagraph images. These height-time points, measured at the position angle (PA) of  $264^{\circ}$ , are plotted in Figure 1. A linear fit (short-dashed line) to these data yielded a plane-of-sky speed of  $2600 \text{ km s}^{-1}$  and a projected liftoff time of 1733 UT, consistent with the first appearance of the CME in the MK4 coronameter at Mauna Loa. Although a second-order fit to the LASCO data indicated a deceleration of  $-32 \text{ m s}^{-2}$  ([http://cdaw.gsfc.nasa.gov/CME\\_list/](http://cdaw.gsfc.nasa.gov/CME_list/)), three points are not sufficient to provide an accurate value for the CME deceleration. However, as we shall see below, such a value for the deceleration is quite consistent with the results of our analyses using the combined white light and radio data that extend beyond the field of view of the LASCO coronagraph.

[16] The CME-driven shock associated with this event arrived at the Wind spacecraft, which was  $177.6 R_E$  down-tail from Earth, at about 0645 UT on 4 November. Since at this time Earth was at 0.9924 AU, the transit time from liftoff on the Sun to arrival at Wind was 37.4 hours, implying an average transit speed of  $1114 \text{ km s}^{-1}$ . This shock was immediately followed by a sheath of enhanced plasma density (reaching  $20 \text{ cm}^{-3}$  at Wind) and an ejecta that arrived about 4 hours later at 1100 UT on 4 November. The height-time values corresponding to the transit speed, projected back to the Sun, are shown by the dotted line in Figure 1. Comparison of the transit speed ( $1114 \text{ km s}^{-1}$ ) with the CME speed measured near the Sun ( $2600 \text{ km s}^{-1}$ ) indicates that the CME must have experienced significant deceleration as it propagated from the Sun to 1 AU.

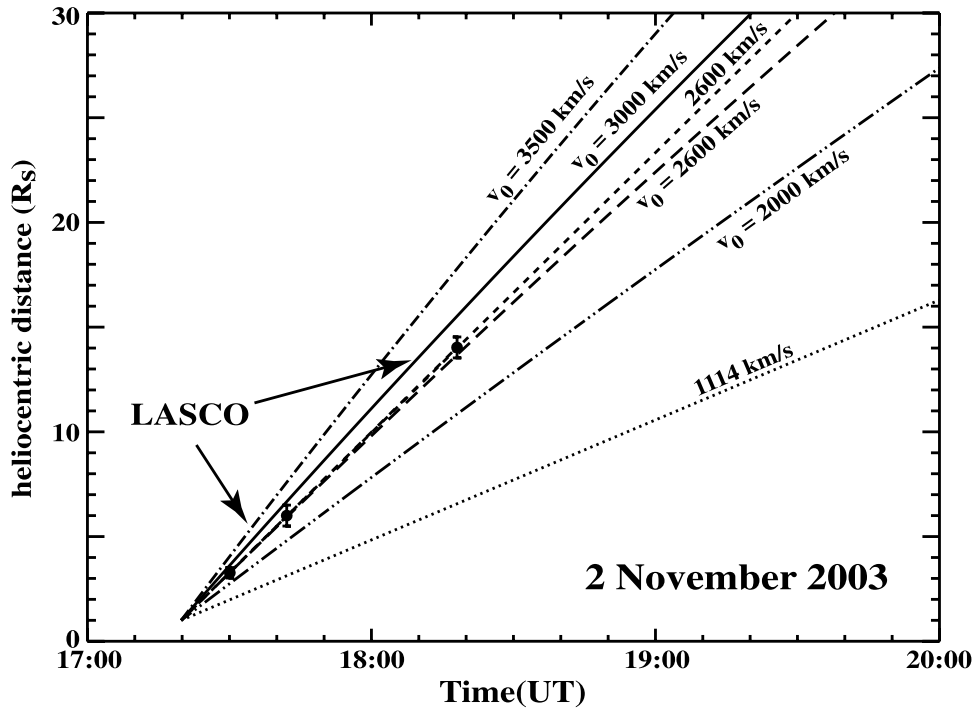


**Figure 1.** Plot of the (plane-of-sky) height-time data for the 2 November 2003 coronal mass ejection (CME) from the SOHO/LASCO coronagraph. The best straight-line fit (short-dashed line) gives a plane-of-sky speed of  $2600 \text{ km s}^{-1}$ . The other lines and curves on the figure are explained in the text.

[17] Figure 2 plots both the heliocentric distance (Figure 2a) and speed (Figure 2b) versus time, deduced for the CME/shock during the entire period of propagation to 1 AU. The dotted and short-dashed lines are the exten-

sion of the lines in Figure 1 that correspond to constant propagation speeds of  $1114 \text{ km s}^{-1}$  and  $2600 \text{ km s}^{-1}$ , respectively. The  $2600 \text{ km s}^{-1}$  line is clearly inconsistent with the arrival time of the CME at 1 AU, while the

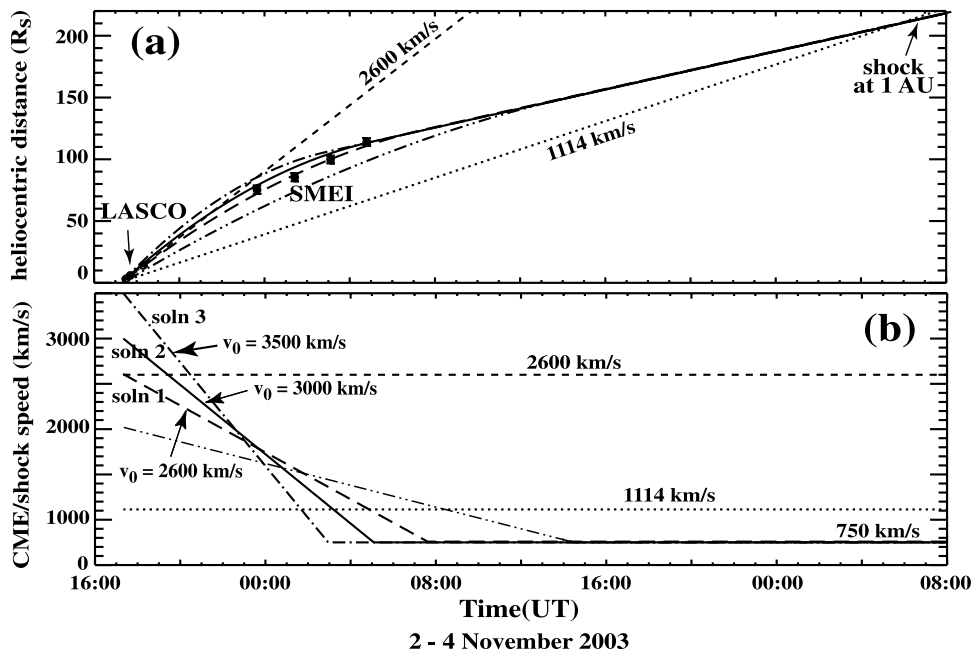


**Figure 2.** Plots of the CME/shock kinematics from the Sun to 1 AU. (a) Plot of the heliocentric distance as a function of time. The data points are the Large-Angle Spectrometric Coronagraph (LASCO) and Solar Mass Ejection Imager (SMEI) white light measurements. (b) Plot of the corresponding CME/shock speed versus the time. The various lines and curves are explained in the text.

1114 km s<sup>-1</sup> line disagrees with the LASCO height-time measurements.

[18] The Abraham-Shrauner method [Abraham-Shrauner and Yun, 1976] was used to estimate the shock parameters at the Wind spacecraft. Using the jump in the plasma parameters across the shock measured by Wind/SWE [Ogilvie et al., 1995] and in the magnetic field values measured by Wind/MFI [Lepping et al., 1995], we determined that this quasi-perpendicular shock, with Alfvén Mach number of 2.7, had a speed of 750 km s<sup>-1</sup>.

[19] Radial speed profiles, relevant for this CME/shock as it propagated through the interplanetary medium, were derived using the technique introduced by Reiner et al. [2001]. This method uses the measured shock parameters at 1 AU, the transit time, and assumes that this fast CME initially decelerated at a constant rate (consistent with LASCO observations), then propagated at a constant (shock) speed of 750 km s<sup>-1</sup> to 1 AU. This latter assumption is consistent with low-frequency radio observations that indicate that CME/shocks, in general, eventually achieve a constant speed as they propagate through the interplanetary medium [Reiner et al., 1998b; Reiner et al., 1999]. Then for any value for the initial CME speed, the measured transit time and 1 AU shock speed yield a unique solution for the entire CME/shock speed profile from the Sun to 1 AU, within the context of this simple deceleration model. For example, for an initial CME radial speed of 2600 km s<sup>-1</sup> (equal to the LASCO plane-of-sky speed), the measured transit time and 1 AU shock speed require that the CME must decelerate at a rate of -35.9 m s<sup>-2</sup> for 14.3 hours, i.e., out to a heliocentric distance of 0.58 AU (125 R<sub>⊙</sub>). This speed profile is shown by the long-dashed line in Figure 2b (referred to as Soln 1). The height-time curve, calculated from this speed profile, is shown by the long-dashed curve in Figure 2a and in Figure 1. Figure 1 shows this solution to be consistent with the LASCO height-time measurements to within their uncertainties and of course it agrees with the 1 AU measurements by construction.

[20] Because of projection effects, the actual CME speed was likely somewhat higher than 2600 km s<sup>-1</sup>. If we make the simplest geometric projection corrections, we would expect that for a CME launched from W56°, a plane-of-sky speed of 2600 km s<sup>-1</sup> would correspond to an initial “true” radial speed of 3000 km s<sup>-1</sup>. This initial CME speed would lead to a somewhat different solution for the speed profile implied by the constraints at 1 AU. A CME with initial speed of 3000 km s<sup>-1</sup> would have to decelerate at a rate of -53.2 m s<sup>-2</sup> for 11.8 hours, i.e., out to a heliocentric distance of 0.53 AU (115 R<sub>⊙</sub>). This latter solution is indicated by the solid curves in Figures 2a and 2b (referred to as Soln 2) and in Figure 1. Likewise, a CME with initial speed of 3500 km s<sup>-1</sup> would have to decelerate at a rate of -79.4 m s<sup>-2</sup> for 9.6 hours, i.e., out to a heliocentric distance of 0.50 AU (107 R<sub>⊙</sub>). This latter solution is indicated by the dot-dashed curves in Figures 2a and 2b (referred to as Soln 3) and in Figure 1. Although for these latter two solutions the height-time values do not pass through the LASCO height-time measurements, they are clearly consistent with them: any CME initial speed higher than the plane-of-sky speed is also consistent with the measured LASCO height-time data.

[21] By contrast, any solution with an initial CME speed lower than 2600 km s<sup>-1</sup>, while consistent with the 1 AU requirements, would be inconsistent with the LASCO measurements and therefore not a viable solution for this CME. As an example, the double-dot-dashed curves in Figures 1 and 2 are the speed and distance profiles, consistent with the 1 AU observations, that would be obtained for this CME if its initial radial speed was 2000 km s<sup>-1</sup>. In this case it would decelerate at a rate of -16.4 m s<sup>-2</sup> for a period of 21.2 hours, i.e., out to a heliocentric distance of 0.70 AU (152 R<sub>⊙</sub>). Although this is not a viable kinematic solution based on the LASCO measurements, it will be interesting to ascertain whether this solution is also ruled out by the SMEI and radio observations discussed below.

[22] It should be noted that the speed and distance profiles determined in this way represent, by construction, the “true” radial speed and (heliocentric) distance. Correspondingly, the value of the acceleration represents the “true” acceleration. By contrast, the second-order fit to the LASCO height-time values gives only the “apparent” acceleration [Yashiro et al., 2004].

[23] The trend of the speed profiles in Figure 2 is clear: a CME with a greater initial speed must decelerate more rapidly, but for a shorter period of time, in order to satisfy the constraints of the 1 AU observations. At this point, there is no way to single out these or any of a whole family of equally valid kinematic solutions for the 2 November 2003 CME. To establish which of these equally valid solutions best represents the actual kinematics of the 2 November 2003 CME, additional observational constraints must be imposed. One obvious additional constraint is provided by the elongation measurements made by the all-sky white light camera on SMEI.

### 3.2. SMEI White-Light Observations

[24] An example of a SMEI white light image for the 2 November 2003 CME is illustrated, in Hammer-Aitoff format, in Figure 3. Since this is a difference image obtained from consecutive spacecraft orbits, the white areas correspond to areas of intense Thomson-scattered light from the current orbit, while the dark areas correspond to areas of intense brightness during the preceding spacecraft orbit. The image cadence of SMEI is 102 min. The CME originated to the southwest, but much of this region was obscured in the SMEI images by the shutter blocking Camera 3 from bright sunlight. In this difference image, the arrow points to the leading edge of the CME, where the elongation angle measurement was made at 0118:05 UT. The curves on the figure are the estimated location of the shock front deduced from the speed profiles in Figure 2 corresponding to an initial speed of 2600 km s<sup>-1</sup> (dashed) and 3000 km s<sup>-1</sup> (solid), respectively. While the location of these shocks near the ecliptic plane were correctly rendered, the shock fronts outside the ecliptic plane were sketched in assuming an approximately spherical shock, the actual latitudinal extent of the shock being unknown.

#### 3.2.1. Analysis of SMEI Solar Elongations

[25] The solar elongations (angle of the CME leading edge measured from the Earth-Sun line) for the SMEI CME are plotted in Figure 4 as a function of the time of the measurement at the CME leading edge. These measure-

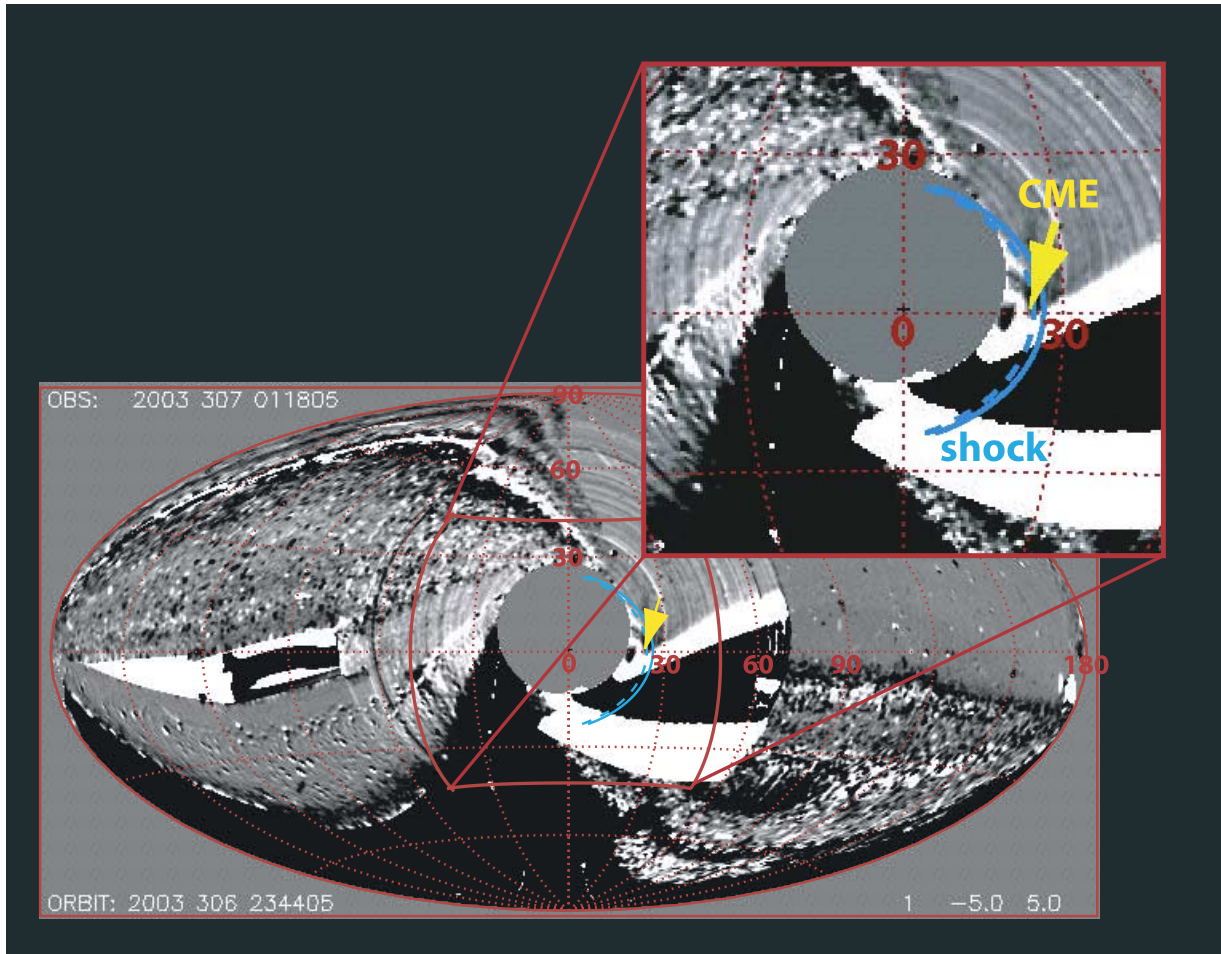


**Figure 3.** SMEI Hammer-Aitoff difference image of the interplanetary CME observed at 0118 UT on the 3 November 2003 CME. The yellow arrow points to the leading edge of the CME. The blue curves are the estimated locations of the shock, as described in the text.

ments were made at a position angle (PA) =  $270^\circ$ , which was sufficiently close to the LASCO measurements at PA =  $264^\circ$ . The uncertainties in measured elongation angles was estimated to be about  $1^\circ$ . Owing to the passage of the CME into the sunlight-saturated region, only four elongation measurements were possible at this position angle. For comparison, we also display the solar elongations,  $\varphi$ , derived from the LASCO plane-of-sky measurements of heliocentric distance,  $R$ :  $\tan \varphi = R$ , where  $\varphi$  is the solar elongation angle.

[26] To determine the solar elongations of the shock front that correspond to the “true” CME kinematics given by the various curves in Figure 2, we assumed an outward moving spherical shock and calculated the (solar elongation) angle to its leading edge as seen from Earth, corresponding to the distance of closest approach to the Sun. The solid, long-dashed, dot-dashed, and double-dot-dashed curves in Figure 4 were derived from the corresponding four decelerating kinematic solutions shown in Figure 2. For comparison, the short-dashed and dotted curves show the solar elongations that correspond to the CME moving at constant speeds of  $2600 \text{ km s}^{-1}$  and  $1114 \text{ km s}^{-1}$  (transit speed), respectively. These latter elongation curves differ significantly from the measured SMEI CME elongations.

[27] While the constant speed shock traveling at  $2600 \text{ km s}^{-1}$  (short-dashed curve) is clearly inconsistent with the measured SMEI elongations, the solar elongations calculated for the kinematic solution (Soln 1), corresponding to an initial “true” speed of  $2600 \text{ km s}^{-1}$  with deceleration to a final speed of  $750 \text{ km s}^{-1}$  at 1 AU (dashed curve), fits both the LASCO and the SMEI elongations to within the measured uncertainties. These results immediately demonstrate that to simultaneously fit the LASCO and SMEI elongations, this CME must have decelerated significantly between the times of the LASCO and SMEI observations.

[28] As pointed out above, projection effects suggest that a solution with an initial CME speed of  $3000 \text{ km s}^{-1}$  is also consistent with the LASCO height-time measurements and, in fact, may better approximate the actual kinematics for this CME. The calculated solar elongations that correspond to this CME kinematic solution (Soln 2) are given by the solid curve in Figure 4. This solution, which yields solar elongations that are somewhat larger than those measured by SMEI, might correspond to the shock moving significantly ahead of the dense plasma that constitutes the white light CME observed by SMEI at these distances from the Sun. The calculated solar elongations that correspond to a

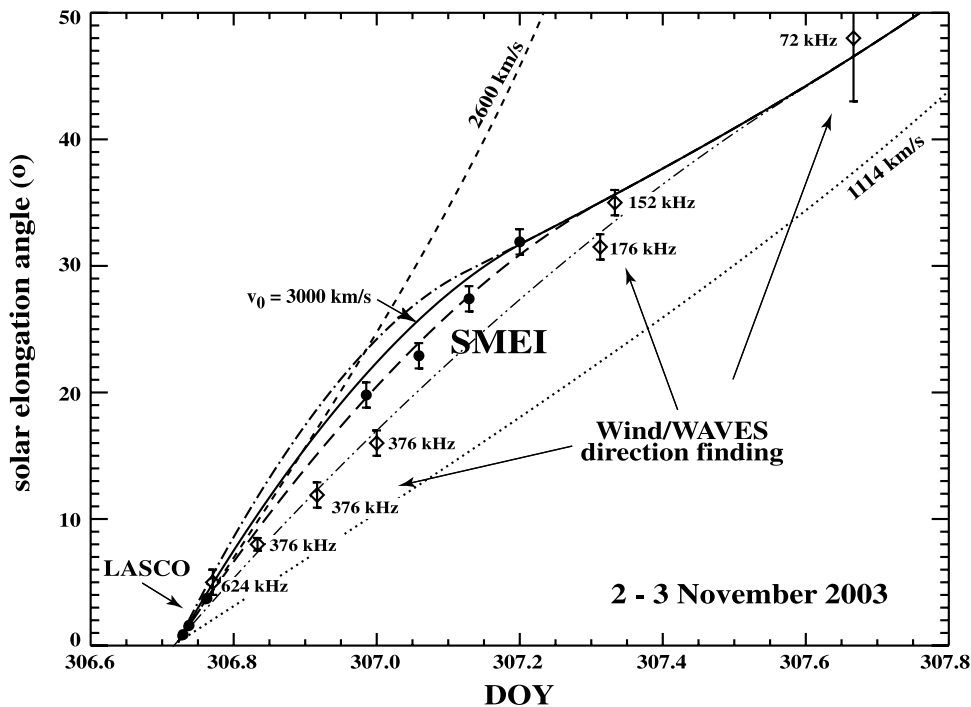


**Figure 4.** Plot of the solar elongation angle as a function of time. The solid points are the solar elongations measured by SMEI and LASCO. The diamonds are the solar elongations derived from the radio source direction finding. The curves are the solar elongations of the leading edge of the (assumed) spherical shock front, corresponding to the various kinematic solutions given in Figure 2.

CME initial speed of  $3500 \text{ km s}^{-1}$  (Soln 3) are also shown by the dot-dashed curve in Figure 4.

[29] Finally, we also show in the double-dot-dashed curve in Figure 4 the kinematic solution corresponding to an initial CME speed of  $2000 \text{ km s}^{-1}$ . Comparison with the measured SMEI elongations shows that this kinematic solution is not only inconsistent with the LASCO measurements but is also clearly inconsistent with the SMEI observations.

[30] As Figure 4 illustrates, it is significant and fortuitous that the SMEI measurements were made at those solar elongations before this CME ceased to decelerate. This means that the SMEI measurements can potentially distinguish between the various decelerating profiles provided by the above analysis: farther from the Sun the CME deceleration ceases so that all the different kinematic solutions that are consistent with the LASCO and 1 AU data coalesce into a common elongation curve that corresponds to constant propagation speed through the interplanetary medium to 1 AU.

### 3.2.2. SMEI Height-Time Values

[31] As for LASCO, the SMEI images provide only plane-of-sky measurements. The heliocentric distances of the CME can therefore be deduced from these SMEI images only when the projection effects are removed. To do this, we adopt the simplest geometric model in which the dense CME material is assumed to move out radially and symmetrically from the flare site at  $W56^\circ$ . Then the height,  $h$ , measured from the center of the Sun, is given by  $h = 1/(\sin B/\tan E + \cos B)$ , where  $B$  is the solar longitude of the flare site and  $E$  is the solar elongation measured by SMEI. The CME heights ( $h$ ) derived in this way from the four

measured SMEI elongations are plotted in Figure 2. They range from  $75 R_\odot$  ( $0.35 \text{ AU}$ ) to  $114 R_\odot$  ( $0.53 \text{ AU}$ ). Figure 2 shows that they are consistent with the height-time profiles derived for a decelerating CME/shock with initial speeds of  $2600 \text{ km s}^{-1}$  or  $3000 \text{ km s}^{-1}$  and possibly  $3500 \text{ km s}^{-1}$ .

[32] Furthermore, we found that if the SMEI material was assumed to have moved out from solar longitudes ( $B$ ) significantly larger or smaller than  $W56^\circ$ , then the derived SMEI heights would lie well above the calculated shock heights given by the various curves in Figure 2. These results suggest that the CME material, observed by SMEI, likely moved radially outward from the Sun between  $W50^\circ$  and  $W60^\circ$ , i.e., near the flare site.

[33] The precise determination of the relevant kinematic solution for the 2 November CME depends on the interpretation of the nature and origin of the SMEI density enhancements. If we interpret the features observed in the SMEI images as corresponding to density enhancements immediately behind the shock front, which may correspond to swept up solar wind plasma, then the SMEI observations would tend to favor Soln 1. If, on the other hand, we suppose that the density enhancements detected by SMEI correspond to CME material well behind the driven shock, then Solns 2 or 3 might be favored. Soln 2, for example, would suggest a shock standoff distance at 0.5 AU of the order of  $7 R_\odot$  or  $0.03 \text{ AU}$  (estimated from Figure 2), which, based on Helios and 1 AU observations, is not unreasonable [e.g., see *Volkmer et al.*, 1982; *Burlaga et al.*, 1981]. The estimated standoff distance observed at 1 AU for this CME is about  $15 R_\odot$  or  $0.07 \text{ AU}$ .

[34] Figures 2 and 4 show that there is a significant gap between the last LASCO measurement and the first SMEI

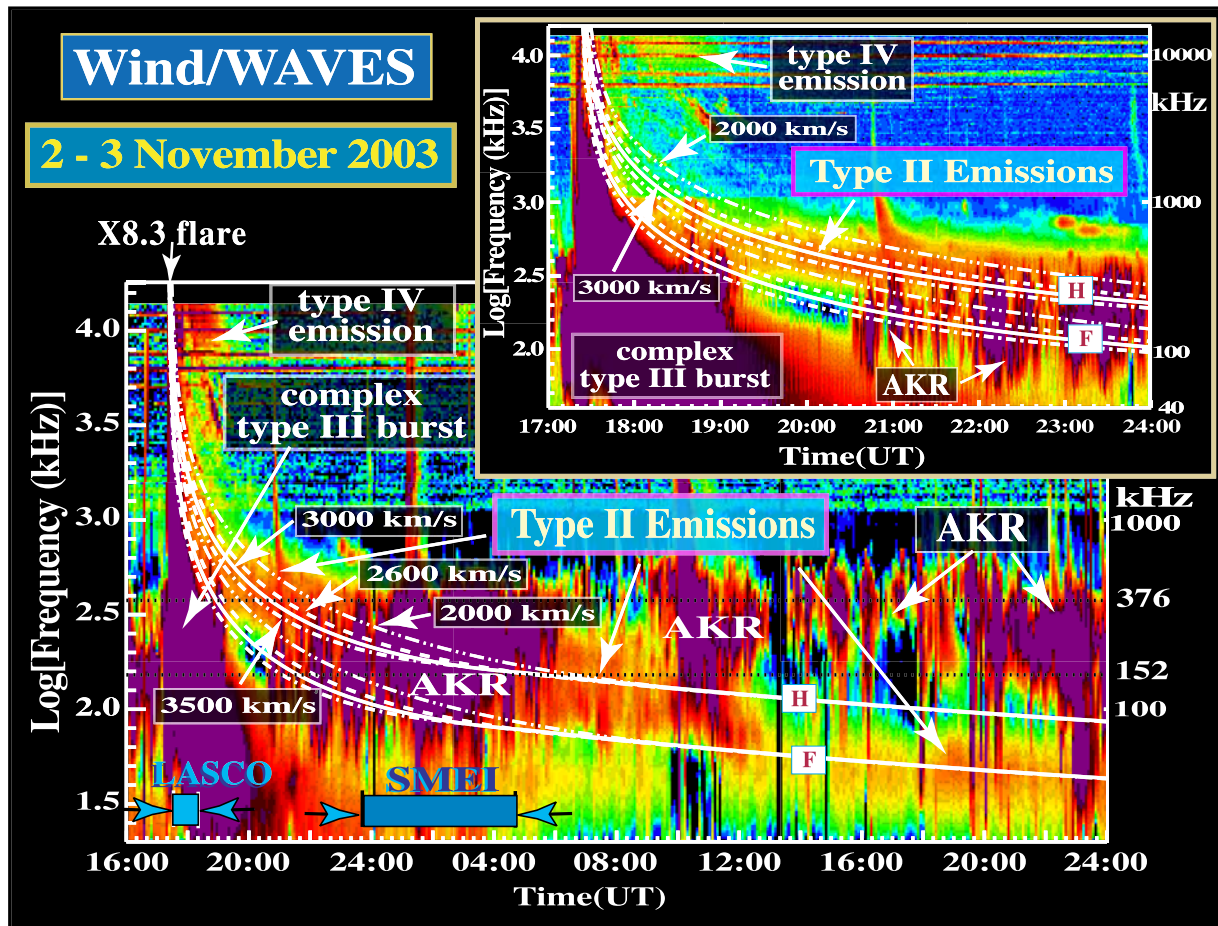


**Figure 5.** Dynamic spectrum of the radio data observed by Wind/WAVES showing the type II and type III radio emissions associated with the 2 November 2003 solar/CME event. The white curves are the frequency–time curves, obtained using the *Saito et al.* [1977] model, that correspond to the various CME/shock kinematic solutions illustrated in Figure 2 and that correspond to a best fit to the frequency drift rate of the type II radio emissions generated by the CME/shock. Each kinematic solution gives two frequency–time curves that correspond to emissions at the fundamental (*F*) and harmonic (*H*) of the plasma frequency. The inset shows, in greater detail, the emissions at the beginning of this event. The dotted black lines show the frequencies where the direction-finding analyses in Figures 6 and 7 were made.

measurement, where there are no white light observations. There is also no white light information for this event beyond  $\sim 0.5$  AU. However, as we will see below, information on the CME kinematics that spans this gap between the LASCO and SMEI observations may be provided by the low-frequency type II radio emissions, generated by the CME-driven shock.

### 3.3. Type II Radio Emissions

[35] The radio emissions observed by Wind/WAVES associated with this major solar event were rather complex. A dynamic spectrum of these radio emissions in the frequency range from  $\sim 20$  kHz to 13.825 MHz is shown in Figure 5. This is a plot of the radio intensity (red being most intense) as a function of frequency (y-axis) and time (x-axis). The time period extends from 1600 UT on 2 November to 2400 UT on 3 November. The inset in the upper right shows, in greater detail, the emissions in the frequency range from 40 kHz to 13.825 MHz from 1700 to 2400 UT on 2 November 2003.

[36] As expected, the solar event initiated a very intense, long-duration, complex type III-like burst generated by electron beams escaping from the flaring region [Reiner and Kaiser, 1999; Reiner et al., 2000a]. This complex type III-like burst was immediately followed by very complex, frequency-drifting type II emissions that were generated by the shock driven by the CME. Because of the high speed of this CME and consequent fast frequency drift rate, these type II emissions are initially difficult to distinguish from the complex type III-like emissions.

[37] Since during this time period, the Wind spacecraft was located far down Earth’s tail region ( $\sim 178 R_E$ ), these low-frequency interplanetary radio emissions of solar origin were further obscured, in the several 100s of kHz frequency range, by intense Auroral Kilometric Radiation (AKR) emissions [Gurnett, 1975], triggered at Earth by this and earlier space weather events.

[38] As can be seen in Figure 5, there were three periods when the type II emissions were particularly evident in the radio data. The first period, at the higher frequencies,

extended from the end time of the complex type III burst until about 2100 UT on 2 November, while drifting down to a frequency of around 350 kHz. The beginnings of this type II emission is somewhat obscured by the preceding intense complex type III emissions. There was then another period from about 0600 to 1000 UT on 3 November (during a hiatus in the AKR emissions) in the frequency range centered around 160 kHz. As our analysis of frequency drift (below) indicates, these type II emissions were generated at the harmonic of the plasma frequency. The final period of type II emissions extended from about 1300 to 2300 UT on 3 November in the frequency range between 50 and 60 kHz. Our analysis below indicates that these emissions were generated at the fundamental of the plasma frequency. As is the case here, fundamental and harmonic kilometric type II emissions for a given solar event are often generated at different times. The total frequency range (from >1 MHz to 50 kHz) over which these type II radio emissions were observed corresponds to the CME/shock propagating from the high coronal to about 0.9 AU.

### 3.3.1. Analysis of the Type II Frequency Drift

[39] The observed frequency drift rate of the type II radio data provides information on the propagation of the CME/shock through the corona and interplanetary medium [Reiner *et al.*, 1998b]. The basic reason is that type II radio emissions are generated by the CME-driven shocks. These emissions occur at the fundamental and harmonic of the plasma frequency,  $f_p$ , which in turn is directly related to the square root of the plasma density,  $n$ , in the source region, i.e., in the corona and interplanetary medium ( $f(\text{kHz}) = f_p = 9 \sqrt{n(\text{cm}^{-3})}$ ). Since the coronal and interplanetary density decreases with increasing heliocentric distance, the CME/shock will generate radio emissions at decreasing frequencies as it propagates through the corona and interplanetary space. Specifically, the measured frequency drift rate at a given time is directly related to the “instantaneous” speed of the the shock driven by the CME.

[40] However, in order to relate the actual speed and distance profiles of the shock to the radio data, it is necessary to know the relationship of the plasma density to the heliocentric distance in the radio source region, i.e., it is necessary to assume a coronal and/or heliospheric density model. A number of such density-distance scales have been derived both from the radio data [Fainberg and Stone, 1971; Leblanc *et al.*, 1998] and from the white light coronagraph observations [Saito, 1970; Saito *et al.*, 1977; Newkirk, 1961, 1967], as well as from direct in situ measurements, for heliocentric distances greater than 0.3 AU [Bougeret *et al.*, 1984]. Fortunately, the results of the analyses provided here are not critically dependent on any chosen density model. Owing to the normal coronal and heliospheric density fluctuations, any given model must be scaled to fit the frequency drift and this scale factor diminishes the differences between the various models, at least for the applications that we have in mind here. For the 2 November CME event, we will determine the appropriate value of this density model scale factor by requiring consistency between the radio and 1 AU in situ observations.

[41] For simplicity, and since we are comparing the radio with white light observations, we use the K-corona model of Saito *et al.* [1977]. This model was chosen primarily because, by construction, it was designed to have the correct

density falloff in the interplanetary medium [Bougeret *et al.*, 1984]. (This model is not expected to be valid in the low corona, but we will not be making any comparisons or analyses in that region).

[42] The technique of Reiner *et al.* [2001] attempts to select that kinematic solution from Figure 2 that provides the best fit to the observed frequency drift of the type II radio emissions that were generated by the propagating CME/shock. Since the speed and distance profiles in Figure 2 represent the “true” radial CME/shock speed and distance, they can be directly compared to the frequency drift of the type II radio emissions, once we have decided on the appropriate density model.

[43] As an illustration, the dashed curves on Figure 5 were obtained from Soln 1 ( $2600 \text{ km s}^{-1}$ ) using the Saito *et al.* [1977] model to convert the heliocentric distance-time curve in Figure 2a to frequency versus time curves. Two curves are obtained that correspond to emission at the fundamental and harmonic of the plasma frequency, with a frequency ratio of 2. The Saito *et al.* [1977] model density was multiplied by a constant scale factor that was varied (by eye) to the centroid of the frequency-drifting bands corresponding to the fundamental and harmonic type II radio emissions in Figure 5. The scale factor that yielded the best fit for this kinematic solution was 1.2. This scaled Saito *et al.* [1977] density model then gives the heliocentric distance of the type II radio source corresponding to any observed frequency for this event. Essentially identical results are obtained if we assume a simple  $n_o/R^2$  model falloff (with  $n_o = 18 \text{ cm}^{-3}$ ), instead of the Saito *et al.* [1977] density model (which falls off as  $1/R^{2.14}$  at large distances). The fact that these curves fit the type II frequency drift over this entire frequency range simple confirms the  $\sim 1/R^2$  average falloff of the interplanetary plasma density. This is expected since the diffuse band of type II radio emissions that are observed for this CME event originate from individual radio sources distributed over a large region of the shock surface. The observed frequency-drift therefore represents an average of the radio emissions generated over a large region of interplanetary space. Consequently, the average frequency-drift of the type II radio emission must follow the average density falloff in the interplanetary medium.

[44] For comparison, we also show in Figure 5, in the solid and dot-dashed curves, the best fit to the frequency drift, obtained using the solutions (Soln 2 and Soln 3) in Figure 2 that correspond to initial CME speeds of  $3000 \text{ km s}^{-1}$  and  $3500 \text{ km s}^{-1}$ , respectively, both obtained with the Saito *et al.* [1977] model, also scaled by the factor of 1.2. This same scale factor is required to assure the these kinematic solutions also pass through the centroid of the fundamental and harmonic type II emission bands at the lower frequencies (below 160 kHz), observed from 0600 to 2400 UT on 3 November. Finally, the double-dot-dashed curves in Figure 5 correspond to the CME kinematics with an initial speed of  $2000 \text{ km s}^{-1}$ .

[45] Since the type II emissions for this event are very complex (consisting of sporadic and multilined structures) and are very wide-banded, it is not easy, in this particular case, to distinguish between these different possible kinematic solutions. However, the solution corresponding to the

initial shock speed of  $2000 \text{ km s}^{-1}$  clearly does not provide a good fit to the radio frequency drift at the higher frequencies. This is most readily seen in the insert in Figure 5 that shows this region in more detail; the double-dot-dashed curves miss the centroid of the intense band of type II emissions between 1830 and  $\sim 2100$  UT (after this point the type II emissions are partly obscured by the “tail” of a weak type III burst and by the stronger AKR emissions observed at that time). No reasonable modification of the scale factor of the *Saito et al.* [1977] density model (or simple  $1/R^2$  model falloff) will yield a frequency-time curve that fits the type II frequency drift over its entire frequency range (from  $>1$  MHz to 50 kHz) for this kinematic solution. Thus not only is this kinematic solution ruled out by the LASCO and SMEI observations but also by the observed frequency drift of the type II radio emissions, in spite of the fact that this solution is consistent with the constraints imposed by the 1 AU observations.

[46] Figure 5 shows that the other three kinematic solutions provide a significantly better fit to the frequency drift of the intense band of type II emissions from about 1900 to 2100 UT on 2 November, while at the same time fitting the centroid of the other two clear episodes of frequency-drifting type II emissions observed below 160 kHz from 0600 UT on 3 November. It is clear from these fits, that the frequency drift that corresponds to an initial CME/shock speed of less than  $2600 \text{ km s}^{-1}$  or greater than  $3500 \text{ km s}^{-1}$  will not provide a good fit to the high-frequency type II emissions. In fact, the kinematic solution corresponding to an initial CME speed of  $3000 \text{ km s}^{-1}$  appears to provide the best fit through the centroid of this wideband emission from about 1900 to 2100 UT on 2 November so that seems to be the kinematic solution favored by the frequency drifting type II emissions observed over this 2-day period. We estimate the uncertainty in this fit to be perhaps  $\pm 200 \text{ km s}^{-1}$ .

### 3.3.2. Direction-Finding Analysis of the Type II Radio Data

[47] There is yet one independent aspect of the radio observations that we have not explored. In addition to the “frequency profile” of the type II emissions, the WAVES receivers on the spinning Wind spacecraft have the capability of measuring the solar elongation of the centroid of the type II radio source. The angular resolution of a simple dipole antenna, however, is not sufficient to provide a radio image that could be directly compared with the SMEI images.

[48] Analysis of the radio signal modulation produced by the spinning dipole antenna on the Wind spacecraft permits the determination of both the full 2-D line-of-sight directions to the centroid of the radio source, the source angular size, and the polarization state of the radio signal. This is done by combining the signals from the spin axis antenna and the spinning dipole antenna in the spacecraft spin plane [Manning and Fainberg, 1980; Fainberg et al., 1985]. The results of the direction-finding analyses are the closest thing that we currently have to a radio image and it is therefore natural to compare these results with the SMEI white light observations.

[49] In Figure 6 we display results of the direction-finding analysis at 376 kHz from 1600 to 2400 UT on 2 November,

which includes the time of the intense type III burst and the weaker type II radio emissions associated with the CME.

[50] Figure 6a shows the derived source intensity in log of solar flux units (sfu) ( $1 \text{ sfu} = 10^{-22} \text{ W m}^{-2} \text{ Hz}^{-1}$ ). The radio intensity is seen to rise very rapidly from the galactic background level at the onset time of the type III burst at about 1720 UT. After about 1900 UT, WAVES detected the weaker signal of the type II emissions.

[51] Figures 6b and 6c show the radio source angular directions deduced from this analysis. These are the line-of-sight directions to the centroid of the radio sources relative to the location of the spinning Wind spacecraft. Since the simple dipole antenna has poor angular resolution, if there are distinct, multiple radio sources, the direction-finding analysis gives the direction angles to the radio centroid of these sources. Figure 6b presents the radio source azimuthal direction, relative to the spacecraft-Sun direction ( $0^\circ$ ): a negative angle implies a source to the east of the Wind-Sun line; a positive angle implies a source to the west of the Wind-Sun line. After 1900 UT the intense type III emissions decreased below the level of the weaker type II emissions and the azimuth of the centroid of the radio sources slowly drifted from about  $W8.0^\circ \pm 0.5^\circ$  to about  $W16^\circ \pm 1^\circ$  by the end of the day (dashed line is shown to guide the eye). This azimuthal drift of the radio centroid results from the motion of the CME-driven shock away from the Sun, as viewed from Earth.

[52] Figure 6c presents the radio source colatitude, measured relative to the spacecraft spin plane (in the case of Wind, the ecliptic plane), derived from the direction-finding analysis for the same time period. Values less than (greater than)  $90^\circ$  correspond to the radio source lying to the north (south) of the ecliptic plane. Figure 6c indicates that the centroid of the type II radio sources were relatively close to the ecliptic plane: sometimes slightly north and other times slightly south of the ecliptic.

[53] Although no image of the radio source is provided by the spinning dipole antenna system on Wind/WAVES, we do obtain an estimate of the overall size of the radio source. Figure 6d presents the source angular radius deduced from the depth of the observed modulation in the antenna signal due to the spin of the spacecraft. Figure 6d indicates that the type II radio source was relatively small, with an angular radius that appears to increase only slightly after 2030 UT from  $\sim 22^\circ$  to  $\sim 27^\circ$  by 2400 UT.

[54] After this time period the weak type II signal, which had drifted down to the frequency range of the AKR, was overwhelmed by the very intense AKR emissions. However, from  $\sim 0600$  to 1000 UT on 3 November, these intense AKR emissions temporarily ceased so WAVES was again able to detect the weak type II emissions, but by this time, owing to the fact that the CME-driven shock was significantly farther from the Sun, they had drifted to significantly lower frequencies, i.e., to lower interplanetary plasma densities. The results of the radio direction finding at 152 kHz are shown in Figure 7, in the same format as in Figure 6. During this time the azimuth indicated a type II radio source centroid at a solar elongation of about  $W31.5^\circ \pm 1^\circ$  and somewhat below the ecliptic plane. The source angular size had increased to  $\sim 35^\circ$ , reflecting, in large part, the fact that the shock,

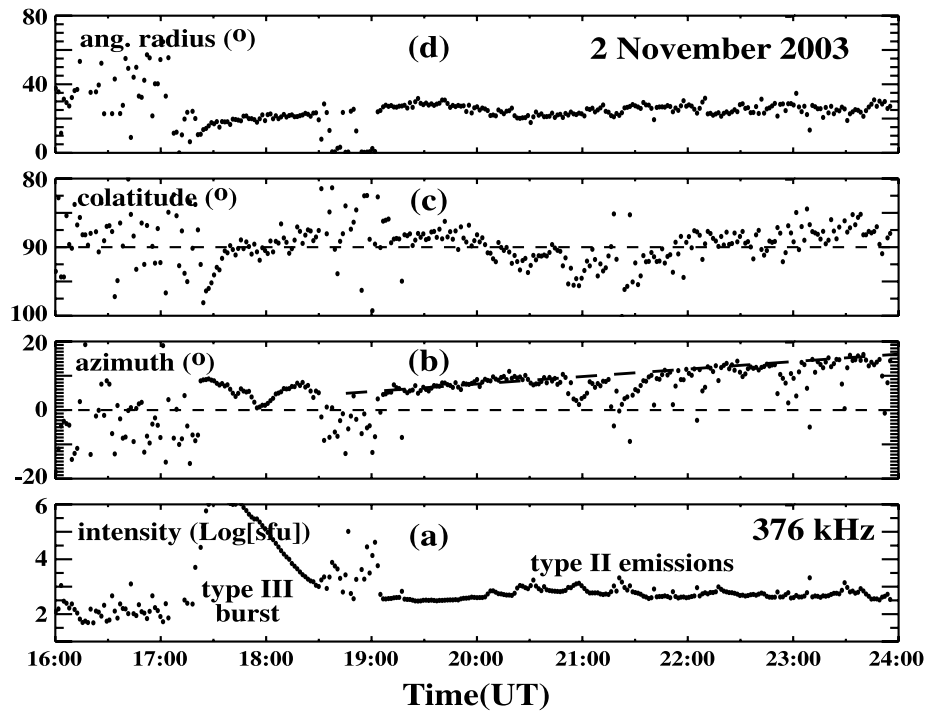


**Figure 6.** Results of the radio direction finding at 376 kHz from 1600 to 2400 UT on 2 November 2003. See text for an explanation of the various panels.

and therefore associated radio sources, was closer to Earth so that its surface subtended a larger angle from Earth.

**3.3.2.1. Comparison With the SMEI Solar Elongations**  
 [55] Since the direction-finding yields a solar elongation angle of the centroid of the radio source, it can

be directly compared with the plane-of-sky solar elongation of the CME leading edge measured by SMEI. The azimuthal or elongation angles for the radio source centroids at various times (and frequencies), derived from the Wind/WAVES direction-finding analyses (as in Figures 6 and 7),

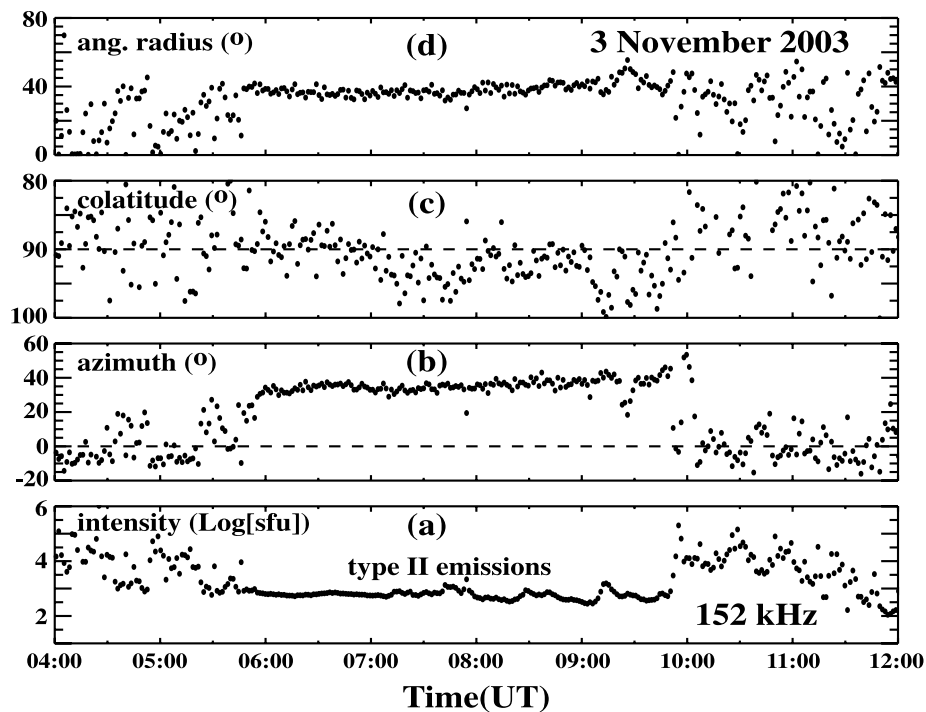


**Figure 7.** Results of the radio direction finding at 152 kHz from 0400 to 1200 UT on 3 November 2003. Same format as Figure 6.

**Table 1.** Derived Longitudes of Radio Sources on the Shock Surface

Frequency, kHz	Time, DOY	Heliocentric Distance, AU	Radio Source Elongation	Radio Source Longitude
624	306.771	0.084	4.5°	65°
376	306.833	0.178	8.0°	43°
376	306.917	0.288	12.0°	34°
376	307.0	0.380	16.0°	31°
176	307.313	0.574	31.5°	34°
152	307.333	0.583	35.0°	45°

are shown by the diamonds on the elongation plot in Figure 4, with their estimated uncertainties. Since the radio direction-finding analysis can also be carried out at higher frequencies, corresponding to solar elongations within the field of view of the LASCO coronagraph, we have also used the radio direction-finding techniques to measure the solar elongations at other radio frequencies, ranging from 624 to 72 kHz. These are also displayed in Table 1 and on Figure 4.

[56] Although these radio elongations cannot be used to precisely locate the leading edge of the shock, primarily due to the finite size of the radio source, they do provide a consistency check on the previous results and provide insights into the locations of radio sources on the shock surface. In spite of the large scatter in these radio elongations, it is reassuring that they were all found to be located near or below the elongations that correspond to the projected shock front for the different kinematic solutions given by the various curves in Figure 4. The radio elongations at the higher frequencies, i.e., 624 and 376 kHz, obtained when the shock was close to the Sun and therefore significantly smaller, as viewed from Earth, are expected to more accurately represent the elongation of the shock. In addition to providing a consistency check, these radio elongations also help to fill the spatial gap between the LASCO and SMEI white light observations.

### 3.3.2.2. Locations on the Shock Front

[57] While the centroid of the type II radio sources is expected to be near the nose of the driven shock, the individual radio sources are likely distributed over a wide area of the shock front. The observer at Earth will view these sources from different perspectives as the shock propagates through interplanetary space and will generally find the centroid of the radio emissions to lie below the leading edge of the shock, projected onto the plane of the sky, as in Figure 4. However, this does not imply that the radio sources are actually located at heliocentric distances less than that of the shock front. Rather, these results reflect the fact that as viewed by an observer at Earth, the type II radio source centroids are likely located at different longitudes along the large, approximately spherical, shock front, and therefore only appear to be behind the shock front. For example, if we assume that the spherical shock surface corresponded to the solution with CME initial speed of  $3000 \text{ km s}^{-1}$ , then at 0000 UT on 3 November the shock would be at 0.380 AU. At that time, the measured elongation of the centroid of the type II radio source at 376 kHz was found to be  $E = W16^\circ \pm 1^\circ$ , observed from Earth (see Figure 4). If we assume this source to lie on the shock surface, then using the simple geometrical

relation given in section 3.2.2, we find that this corresponds to the source centroid on the shock surface at a solar longitude,  $B = W31^\circ \pm 3^\circ$ , i.e., significantly closer to the longitude of Earth than the flare site.

[58] Similarly, we have calculated the solar longitudes corresponding to the other measured radio source elongations at different times and different frequencies, as shown in Figure 4. The results, which are displayed in Table 1, indicate that for this kinematic shock solution the type II source centroids are distributed along the shock front at solar longitudes ranging from  $W30^\circ$  to  $W65^\circ$ , with a clear preference for solar longitudes less than that of the flare site ( $W56^\circ$ ). This is in fact expected since for this western event proximity effects are expected to play a significant role, individual sources on the shock front that are closer to the observer are more intense due to the  $1/R^2$  falloff of the radiation and therefore effectively shift the radio source centroid “below” the projected leading edge of the spherical shock, as viewed from Earth [Reiner and Stone, 1988]. It is expected that these proximity effects will be less important at the higher frequencies when the shock is closer to the Sun and therefore farther from the observer. This may explain why the directions-finding results give solar elongations that are closer to the elongation of the leading edge of the shock near the Sun, e.g., at 624 kHz.

## 4. Discussion

[59] The methodologies described in this paper can provide a quantitative reconstruction of the actual speed and distance profiles of the CME as it propagates from the Sun to 1 AU. The basic reason is that while the white light observations are directly related to the plane-of-sky motion, the frequency-drifting radio observations relate directly to the radial distance. Hence requiring self-consistency between the two different but complementary data sets should, in principle, allow the determination of the “true” CME kinematics.

[60] In practice, however, each data set has uncertainties and limitations that make unambiguous and accurate deductions difficult. The white light observations are always plagued by uncertain projection effects. Also, a relatively large spatial gap exists between the LASCO and SMEI fields of view, where there are no white light observations. The lack of continuity between LASCO and SMEI observations can make it difficult to unambiguously reconstruct the kinematics of a CME, especially in cases where there is significant CME deceleration. Finally, for many cases (like the one investigated here) the SMEI CME is observed and tracked over only a limited range of solar elongations, making it difficult to establish the CME kinematics beyond the SMEI field of view.

[61] On the other hand, the radio frequency observations are always plagued by the uncertainties of the density model that is needed to relate the observed radio frequency to a heliocentric distance. Furthermore, the CME/shock-generated radio emissions are often very complex and their frequency-drift profiles are not always precisely defined. For a spherically symmetric, uniform interplanetary density falloff, the frequency drift of the type II emissions would be expected to follow well-defined, relatively narrow curves at the fundamental and harmonic of the plasma frequency,

since all radio sources distributed over the shock front would experience the same density-distance profile. However, interplanetary density fluctuations across the shock front cause different radio source regions on the shock front to experience somewhat different plasma environments. One simplified way to think of this is that the different radio source regions correspond to different frequency-time curves, each exhibiting a  $1/R^2$  falloff, but with a somewhat different scale factor. The contributions from all the radio sources then gives a family of essentially parallel frequency-time curves: this is just the observed frequency bandwidth of the type II emissions. In reality, the situation is of course more complex because a given radio source on the shock surface does not continue emitting for the duration of the interplanetary propagation. Rather, the different radio sources on the shock front can turn on and off and can intensify at different times during the shock transport through the interplanetary density fluctuations. Such interplanetary density and radio source intensity fluctuations across the shock surface can also make the direction-finding results difficult to interpret.

[62] It is precisely because of these difficulties and limitations of the individual data sets that we have advocated imposing self-consistency of the combined white light, radio, and in situ observations (when available). This can reduce the effects of the uncertainties and limitations in each of the data sets separately and therefore lead to a more robust determination of the complete CME kinematics from Sun to 1 AU.

[63] The analyses for the 2 November event suggest that for fast, decelerating CMEs the SMEI white light observations (from about  $70 R_{\odot}$ ) include the spatial range where, apparently, these fast CMEs transition from approximately constant deceleration to approximately constant speed of propagation. The methodology describe here therefore provides one way to quantify the kinematic characteristics of the CME in this transition region, which is crucially important for space weather predictions. Although this transition region is surely not as abrupt as our model implies, we expect that our simplified kinematic model provides a reasonable approximate representation.

[64] As we have seen, a relatively large spatial gap exists between the end of the LASCO and beginning of the SMEI fields of view. Both the radio frequency drift and the radio direction finding of the type II emissions can help to extend the data coverage across this gap and therefore provide continuity of the CME propagation between the SMEI and LASCO observations. The boxes at the bottom of the dynamic spectrum in Figure 5 show the ranges of the LASCO and SMEI coverage, compared with the radio data. It is seen there that the frequency-drifting type II emissions are clearly defined exactly during the time period of this spatial gap between the LASCO and SMEI observations. The SMEI observations for this event, on the other hand, were made exactly at the time of the very intense AKR emissions, which completely obscured the type II emissions. Also for this event, the SMEI observations extended only out to about 0.5 AU, while the frequency-drifting type II emissions reappeared immediately after the SMEI observations and continued at least until the end of the day on 3 November, corresponding to propagation of the CME/shock to a heliocentric distance of nearly 0.9 AU. Thus

while LASCO and SMEI provide crucially important direct observations of the CME over a relatively small spatial range, the complementary frequency-drifting radio data for this event extend over the entire period of CME propagation from the solar corona to 1 AU. Consequently, in addition to providing a framework for converting the plane-of-sky white light measurements to radial distances, the frequency-drifting radio observations are crucially important for unambiguously establishing the complete CME kinematics. As we have also seen, the direction-finding results can also provide complementary, albeit more limited, observations in the gap between the LASCO and SMEI observations, as well as beyond the SMEI observations. Thus for this event the SMEI white light and radio observations nicely complement each other and together provide essentially continuous data coverage of the 2 November 2003 CME from the solar corona all the way to 1 AU.

[65] Another difficulty of determining the CME kinematics from the direct comparisons of the white light SMEI and radio observations is that these two observations relate to different physical aspects of the CME and its driven shock. A number of different observations suggest that the type II radio emissions are generated just upstream of the CME-driven shock [Reiner et al., 1997; Lengyel-Frey et al., 1997; Thejappa et al., 1997; Bale et al., 1999]. Type II theories also favor upstream generation [Cairns, 1986; Knock et al., 2001]. The SMEI observations presumably relate to the dense CME material, but is this dense swept-up solar wind material that is usually observed just behind the shock, when observed in situ, or is this dense material of the CME itself that may lie well behind the driven shock? This ultimately reduces to the question of the standoff distance of the shock relative to the piston CME driver. Indeed, for the event analyzed here the fact that the radio observations seem to favor the kinematic solution with initial CME speed of  $3000 \text{ km s}^{-1}$ , while the best fit to the SMEI elongations corresponds to the kinematic solution with an initial CME speed of  $2600 \text{ km s}^{-1}$  may suggest that the difference is related to the standoff distance of the shock, relative to the CME driver.

[66] If the SMEI observations relate to the dense CME material, while the radio observations relate to the shock driven by this piston material, then the combined radio, in situ, and white light observations have the potential of actually quantifying the evolution of the CME/shock standoff distance through the interplanetary medium. However, any definite conclusion will require the analyses of more mutual SMEI/WAVES CME events. Similarly, combined white light and radio observations from the upcoming STEREO mission may provide a means of even more directly and accurately determining the evolution of the CME/shock standoff distance during the interplanetary transport of CMEs.

[67] Although this paper has focused on comparison between SMEI and WAVES that can provide information on the interplanetary shock kinematics, the SMEI and WAVES comparisons can, in principle, also provide information other than on the kinematics of CMEs. For example, the 3-D reconstruction techniques can provide information on the plasma density and heliocentric distances of individual “blobs” that constitute the CME [Jackson et al., 2005a]. Since the observed radio frequency of the type II emissions

also directly measures the density in the source region and since the direction-finding analyses and frequency drift provide information on the heliocentric distances, these synergetic observations can be directly compared and are expected to lead to many new insights into how radio sources on the CME shock front relate to structures in the CME and in the interplanetary medium. These investigations will provide the bases for future SMEI/WAVES collaborations.

## 5. Conclusions

[68] It has been known for a long time that CMEs must decelerate as they propagate through interplanetary space. However, until recently there has been only limited progress in quantifying the deceleration profiles of CMEs, primarily due to the lack of direct, dedicated observations.

[69] In this paper, we have attempted to show how the combined white light observations from LASCO and SMEI, the radio observations from Wind/WAVES, and the in situ shock parameters can be used to deduce the radial speed and distance profiles for a CME as it propagates from the Sun to Earth. We have shown that when these observation are combined many of the ambiguities and uncertainties inherent in each are reduced, leading to a more robust determination of the CME kinematics through interplanetary space.

[70] The distance and time over which a CME decelerates depends on the initial CME speed and on the conditions in the interplanetary medium and will differ from one CME event to another. The methodology presented in this paper provides a framework for estimating where and when a given CME essentially stops decelerating. The method introduces a simple kinematic model, then uses all available observational data to constrain the parameters of the model that describe the magnitude and duration of the CME deceleration.

[71] For the 2 November 2003 CME/flare event analyzed here, we have shown that a constant speed solution is inconsistent with both the SMEI white light and type II radio observations. Decelerating solutions with initial CME speeds less than about  $2600 \text{ km s}^{-1}$  were also ruled out by each of the LASCO, SMEI, and radio observations. On the other hand, consistency with each of the LASCO, SMEI, and radio observations and the 1 AU constraints suggested that decelerating solutions with initial CME speeds ranging from  $2600$  to  $3000 \text{ km s}^{-1}$  provide viable solutions for the CME propagation from the Sun to 1 AU. More detailed examination suggests that while the SMEI observations were consistent with solutions with initial CME speed between  $2600$  and  $3000 \text{ km s}^{-1}$  that decelerated to about half an AU, the radio observations appeared to prefer the  $3000 \text{ km s}^{-1}$  solution. The differences may be a consequence of the shock standoff distance. Analyses, such as those performed here, on other mutual SMEI/radio events are expected to provide a better understanding of the relationship between the white light CME and the associated driven shock, as well as their evolution through interplanetary space.

[72] **Acknowledgments.** The Wind/WAVES experiment is a collaboration of NASA/Goddard Space Flight Center, the Observatoire de Paris-Meudon, and the University of Minnesota. SMEI was designed and constructed by a team of scientists and engineers from the U.S. Air Force Research Laboratory, the University of California at San Diego,

Boston College, Boston University, and the University of Birmingham in England. SOHO is a project of international cooperation between ESA and NASA. MJR acknowledges support, in part, from the NSF grant ATM-0417695. For this work DFW and DRM were supported by the Air Force under contract AF19628-00-C-0073. BVJ was supported by NSF grants ATM-0208443 and ATM-0331513 and NASA grant NAG5-134543. The 2 November 2003 CME height-time data were obtained from the CME catalogue generated and maintained by NASA and the Catholic University of America in cooperation with the Naval Research Laboratory.

[73] Arthur Richmond thanks the reviewers for their assistance in evaluating this paper.

## References

- Abraham-Shrauner, B., and S. H. Yun (1976), Interplanetary shocks seen by Ames Plasma Probe on Pioneer 6 and 7, *J. Geophys. Res.*, **81**, 2097.
- Bale, S. D., M. J. Reiner, J.-L. Bougeret, M. L. Kaiser, S. Krucker, D. E. Larson, and R. P. Lin (1999), The source region of an interplanetary type II radio burst, *Geophys. Res. Lett.*, **26**, 1573.
- Bougeret, J. L., J. H. King, and R. Schwenn (1984), Solar radio bursts and in situ determination of interplanetary electron density, *Solar Phys.*, **90**, 401.
- Bougeret, J.-L., et al. (1995), Waves: The Radio and Plasma Wave Investigation on the Wind spacecraft, *Space Sci. Rev.*, **71**, 231.
- Bougeret, J.-L., et al. (1998), A shock associated (SA) radio event and related phenomena observed from the base of the solar corona to 1 AU, *Geophys. Res. Lett.*, **25**, 2513.
- Burlaga, L., E. Sittler, F. Mariani, and R. Schwenn (1981), Magnetic loop behind an interplanetary shock: Voyager, Helios, and IMP 8 observations, *J. Geophys. Res.*, **86**, 6673.
- Cairns, I. H. (1986), The source of free energy for type II solar radio bursts, *Proc. Astron. Soc. Aust.*, **6**, 444–446.
- Cane, H. V. (1983), Velocity profiles of interplanetary shocks, in *Solar Wind 5*, edited by M. Neugebauer, *NASA Conf. Publ.*, CP-2280, 703–709.
- Cane, H. V. (2003), Near-relativistic solar electrons and type III radio bursts, *Astrophys. J.*, **598**, 1403.
- Cane, H. V., and W. C. Erickson (2003), Energetic particle propagation in the inner heliosphere as deduced from low-frequency (<100 kHz) observations of type III radio bursts, *J. Geophys. Res.*, **108**(A5), 1203, doi:10.1029/2002JA009488.
- Cane, H. V., R. G. Stone, J. Fainberg, J. L. Steinberg, and S. Hoang (1982), Type II solar radio events observed in the interplanetary medium I: General characteristics, *Solar Phys.*, **78**, 187.
- Cane, H. V., N. R. Sheeley Jr., and R. A. Howard (1987), Energetic interplanetary shocks, radio emission, and coronal mass ejections, *J. Geophys. Res.*, **92**, 9869.
- Cane, H. V., W. C. Erickson, and N. P. Prestage (2002), Solar flares, type III radio bursts, coronal mass ejections, and energetic particles, *J. Geophys. Res.*, **107**(A10), 1315, doi:10.1029/2001JA000320.
- Dulk, G. A., Y. Leblanc, T. S. Bastian, and J.-L. Bougeret (2000), Acceleration of electrons at type II shock fronts and production of shock-accelerated type III bursts, *J. Geophys. Res.*, **105**, 27,343.
- Eyles, C. J., G. M. Simnett, M. P. Cooke, B. V. Jackson, A. Buffington, P. P. Hick, N. R. Waltham, J. M. King, P. A. Anderson, and P. E. Holladay (2003), The Solar Mass Ejection Imager (SMEI), *Solar Phys.*, **217**, 319.
- Fainberg, J., and R. G. Stone (1971), Type III solar radio burst storms observed at low frequencies. III: Streamer density, inhomogeneities, and solar wind speed, *Solar Phys.*, **17**, 392.
- Fainberg, J., S. Hoang, and R. Manning (1985), Measurements of distributed polarized radio sources from spinning spacecraft: Effect of a tilted axial antenna—ISEE-3 application and results, *Astron. Astrophys.*, **153**, 145.
- Gopalswamy, N., A. Lara, R. P. Lepping, M. L. Kaiser, D. Berdichevsky, and O. C. St. Cyr (2000), Interplanetary acceleration of coronal mass ejections, *Geophys. Res. Lett.*, **27**, 145–148.
- Gopalswamy, N., A. Lara, S. Yashiro, M. L. Kaiser, and R. A. Howard (2001a), Predicting the 1-AU arrival times of coronal mass ejections, *J. Geophys. Res.*, **106**, 29,207.
- Gopalswamy, N., S. Yashiro, M. L. Kaiser, R. A. Howard, and J.-L. Bougeret (2001b), Radio signatures of coronal mass ejection interaction: Coronal mass ejection cannibalism?, *Astrophys. J.*, **548**, L91.
- Gopalswamy, N., S. Yashiro, G. Michalek, M. L. Kaiser, R. A. Howard, D. V. Reames, R. Leske, and T. von Roseninge (2002), Interacting coronal mass ejections and solar energetic particles, *Astrophys. J.*, **572**, L103.
- Gosling, J. T., J. R. Asbridge, S. J. Bame, A. J. Hundhausen, and I. B. Strong (1968), Satellite observations of interplanetary shock waves, *J. Geophys. Res.*, **73**, 43.
- Gosling, J. T., E. Hildner, R. M. MacQueen, R. H. Munro, A. I. Poland, and C. L. Ross (1975), Direct observations of a flare related coronal and solar wind disturbance, *Solar Phys.*, **40**, 439.

- Gurnett, D. A. (1975), The Earth as a radio source: The nonthermal continuum, *J. Geophys. Res.*, *80*, 2751.
- Jackson, B. V., and P. P. Hick (2004), Three-dimensional tomography of interplanetary disturbances, in *Solar and Space Weather Radiophysics Current Status and Future Developments, ASSL 314*, edited by D. G. Gary and C. U. Keller, p. 355, Springer, New York.
- Jackson, B. V., A. Buffington, P. P. Hick, X. Wang, and D. Webb (2005a), Preliminary 3-D analysis of the heliospheric response to the 28 October 2003 CME using SMEI white light observations, *J. Geophys. Res.*, doi:10.1029/2004JA010942, in press.
- Jackson, B. V., et al. (2005b), The Solar Mass Ejection Imager (SMEI) mission, *Solar Phys.*, *225*, 177.
- Knock, S. A., I. H. Cairns, P. A. Robinson, and Z. Kuncic (2001), Theory of type II radio emission from the foreshock of an interplanetary shock, *J. Geophys. Res.*, *106*, 25,041.
- Leblanc, Y., G. A. Dulk, and J.-L. Bougeret (1998), Tracing the electron density from the corona to 1 AU, *Solar Phys.*, *183*, 165.
- Leblanc, Y., G. A. Dulk, M. L. Kaiser, and J.-L. Bougeret (1999), Type U burst and CME in the solar wind, *Geophys. Res. Lett.*, *26*, 1089.
- Leblanc, Y., G. A. Dulk, I. H. Cairns, and J.-L. Bougeret (2000), Type II flare continuum in the corona and solar wind, *J. Geophys. Res.*, *105*, 18,215.
- Lengyel-Frey, D., G. Thejappa, R. J. MacDowall, R. G. Stone, and J. L. Phillips (1997), Ulysses observations of wave activity at interplanetary shocks and implications for type II radio bursts, *J. Geophys. Res.*, *102*, 2611.
- Lepping, R. P., et al. (1995), The Wind magnetic field investigation, *Space Sci. Rev.*, *71*, 207.
- Manning, R., and J. Fainberg (1980), A new method of measuring radio source parameters of a partially polarized distributed source from spacecraft observations, *Space Sci. Instrument.*, *5*, 161.
- Manoharan, P. K., M. Tokumaru, M. Pick, P. Subramanian, F. M. Ipavich, K. Schenk, M. L. Kaiser, R. P. Lepping, and A. Vourlidas (2001), Coronal mass ejection of 2000 July 14 flare event: Imaging from near-Sun to Earth environment, *Astrophys. J.*, *559*, 1180.
- Michalek, G., N. Gopalswamy, A. Lara, and P. K. Manoharan (2004), Arrival time of halo coronal mass ejections in the vicinity of the Earth, *Astron. Astrophys.*, *423*, 729.
- Newkirk, G., Jr. (1961), The solar corona in active regions and the thermal origin of the slowly varying component of solar radio radiation, *Astrophys. J.*, *133*, 983.
- Newkirk, G., Jr. (1967), Structure of the solar corona, *Annu. Rev. Astron. Astrophys.*, *5*, 213.
- Ogilvie, K. W., et al. (1995), SWE, A comprehensive plasma instrument for the Wind spacecraft, *Space Sci. Rev.*, *71*, 55.
- Payne-Scott, R., D. E. Yabsley, and J. G. Bolton (1947), Relative times of arrival of bursts of solar noise on different radio frequencies, *Nature*, *160*, 256.
- Reiner, M. J., and M. L. Kaiser (1999), Complex type III-like radio emissions observed from 1 to 14 MHz, *Geophys. Res. Lett.*, *26*, 397.
- Reiner, M. J., and M. L. Kaiser (2002), CME dynamics in the corona and interplanetary medium from remote radio observations and in situ measurements, *Eos Trans. AGU*, *83*(19), Spring Meet. Suppl., S268.
- Reiner, M. J., and R. G. Stone (1988), Model interpretation of type III radio burst characteristics. I - Spatial aspects, *Astron. Astrophys.*, *206*, 316.
- Reiner, M. J., M. L. Kaiser, J. Fainberg, J.-L. Bougeret, and R. G. Stone (1997), Remote radio tracking of interplanetary CMEs, in *Proceedings of 31st ESLAB Symposium, ESA SP-415*, pp. 183–188, ESTEC, Noordwijk, Netherlands.
- Reiner, M. J., M. L. Kaiser, J. Fainberg, J.-L. Bougeret, and R. G. Stone (1998a), On the origin of radio emissions associated with the January 6–11, 1997, CME, *Geophys. Res. Lett.*, *25*, 2493.
- Reiner, M. J., M. L. Kaiser, J. Fainberg, and R. G. Stone (1998b), A new method for studying remote type II radio emissions from coronal mass ejection-driven shocks, *J. Geophys. Res.*, *103*, 29,651.
- Reiner, M. J., M. L. Kaiser, J. Fainberg, and R. G. Stone (1999), Remote radio tracking of CMEs in the solar corona and interplanetary medium, in *Solar Wind 9*, edited by S. Habbal et al., *AIP Conf. Proc.*, *471*, 653–656.
- Reiner, M. J., M. Karlický, K. Jiříčka, H. Aurass, G. Mann, and M. L. Kaiser (2000a), On the solar origin of complex type III-like radio bursts observed at and below 1 MHz, *Astrophys. J.*, *530*, 1049.
- Reiner, M. J., M. L. Kaiser, S. P. Plunkett, N. P. Prestage, and R. Manning (2000b), Radio tracking of a white-light coronal mass ejection from solar corona to interplanetary medium, *Astrophys. J.*, *529*, L53.
- Reiner, M. J., M. L. Kaiser, M. Karlický, K. Jiříčka, and J.-L. Bougeret (2001), Bastille Day event: A radio perspective, *Solar Phys.*, *204*, 123.
- Reiner, M. J., A. Vourlidas, O. C. St. Cyr, J. T. Burkepile, R. A. Howard, M. L. Kaiser, N. P. Prestage, and J.-L. Bougeret (2003a), Constraints on coronal mass ejection dynamics from simultaneous radio and white-light observations, *Astrophys. J.*, *590*, 533.
- Reiner, M. J., M. L. Kaiser, and J.-L. Bougeret (2003b), On the deceleration of CMEs in the corona and interplanetary medium deduced from radio and white-light observations, in *Solar Wind 10*, edited by M. Velli, R. Bruno, and F. Malara, *AIP Conf. Proc.*, *679*, 152–155.
- Robinson, R. D. (1985), Velocities of type II solar radio events, *Solar Phys.*, *95*, 343–357.
- St. Cyr, O. C., et al. (2000), Properties of coronal mass ejections: SOHO LASCO observations from January 1996 to June 1998, *J. Geophys. Res.*, *105*, 18,169.
- Saito, K. (1970), A non-spherical axisymmetric model of the solar K corona of the minimum type, *Annu. Tokyo Astron. Obs. Ser.*, *2*, 12, 53.
- Saito, K., A. I. Poland, and R. H. Munro (1977), A study of the background corona near solar minimum, *Solar Phys.*, *55*, 121.
- Schwenn, R. (1983), Direct correlations between coronal transients and interplanetary disturbances, *Space Sci. Rev.*, *34*, 85.
- Tappin, S. J., et al. (2004), Tracking a major interplanetary disturbance with SMEI, *Geophys. Res. Lett.*, *31*, L02802, doi:10.1029/2003GL018766.
- Thejappa, G., R. J. MacDowall, and A. F. Vinas (1997), In situ wave phenomena in the upstream and downstream regions of interplanetary shocks: Implications for type II burst theories, in *Proceedings of 31st ESLAB Symposium, ESA SP-415*, pp. 189–194, ESTEC, Noordwijk, Netherlands.
- Volkmer, P. M., F. M. Neubauer, and R. Schwenn (1982), Observation of flare-generated shock waves by Helio-2 near the Sun, *Space Sci. Rev.*, *32*, 131.
- Wild, P. (1954), Radio evidence of the ejection of very fast particles from the Sun, *Nature*, *173*, 532.
- Woo, R., J. W. Armstrong, N. R. Sheeley Jr., R. A. Howard, M. J. Koomen, and D. J. Michels (1985), Doppler scintillation observations of interplanetary shocks within 0.3 AU, *J. Geophys. Res.*, *90*, 154.
- Yashiro, S., N. Gopalswamy, G. Michalek, O. C. St. Cyr, S. P. Plunkett, N. B. Rich, and R. A. Howard (2004), A catalog of white light coronal mass ejections observed by the SOHO spacecraft, *J. Geophys. Res.*, *109*, A07105, doi:10.1029/2003JA010282.

J.-L. Bougeret, Observatoire de Paris, Laboratoire d'Etudes Spatiales et d'Instrumentation en Astrophysique, F-92190 Meudon, France.

B. V. Jackson, Center for Astrophysics and Space Sciences, University of California, San Diego, CA 92093, USA.

M. L. Kaiser, Solar System Exploration Division, NASA Goddard Space Flight Center, Greenbelt, MD 20771, USA.

D. R. Mizuno and D. F. Webb, Institute for Scientific Research, Boston College, Chestnut Hill, MA 02467, USA.

M. J. Reiner, Catholic University of America and NASA Goddard Space Flight Center, Code 695, Greenbelt, MD 20771, USA. (reiner@urap.gsfc.nasa.gov)